

Large anomalous Nernst effect at room temperature in a chiral antiferromagnet

Muhammad Ikhlas^{1†}, Takahiro Tomita^{1†}, Takashi Koretsune^{2,3}, Michi-To Suzuki², Daisuke Nishio-Hamane¹, Ryotaro Arita^{2,4}, Yoshichika Otani^{1,2,4} and Satoru Nakatsuji^{1,4★}

A temperature gradient in a ferromagnetic conductor can generate a transverse voltage drop perpendicular to both the magnetization and heat current. This anomalous Nernst effect has been considered to be proportional to the magnetization^{1–7}, and thus observed only in ferromagnets. Theoretically, however, the anomalous Nernst effect provides a measure of the Berry curvature at the Fermi energy^{8,9}, and so may be seen in magnets with no net magnetization. Here, we report the observation of a large anomalous Nernst effect in the chiral antiferromagnet Mn₃Sn (ref. 10). Despite a very small magnetization $\sim 0.002 \mu_B$ per Mn, the transverse Seebeck coefficient at zero magnetic field is $\sim 0.35 \mu\text{VK}^{-1}$ at room temperature and reaches $\sim 0.6 \mu\text{VK}^{-1}$ at 200 K, which is comparable to the maximum value known for a ferromagnetic metal. Our first-principles calculations reveal that this arises from a significantly enhanced Berry curvature associated with Weyl points near the Fermi energy¹¹. As this effect is geometrically convenient for thermoelectric power generation—it enables a lateral configuration of modules to cover a heat source⁶—these observations suggest that a new class of thermoelectric materials could be developed that exploit topological magnets to fabricate efficient, densely integrated thermopiles.

Current intensive studies on thermally induced electron transport in ferromagnetic materials have opened various avenues for research on thermoelectricity and its application^{12–15}. This trend has also triggered renewed interest in the anomalous Nernst effect (ANE) in ferromagnetic metals^{3–7,15}, which is the spontaneous transverse voltage drop induced by heat current and is known to be proportional to magnetization (Fig. 1a). On the other hand, the recent Berry phase formulation of the transport properties has led to the discovery that a large anomalous Hall effect (AHE) may arise not only in ferromagnets, but in antiferromagnets and spin liquids, in which the magnetization is vanishingly small^{10,16–22}. As the first case in antiferromagnets, Mn₃Sn has been experimentally found to exhibit a large AHE¹⁰. While the AHE is obtained by an integration of the Berry curvature for all of the occupied bands, the ANE is determined by the Berry curvature at E_F (refs 8,9). Thus, the observation of a large AHE does not guarantee the observation of a large ANE. Furthermore, the ANE measurement should be highly useful to clarify the Berry curvature spectra near E_F and to verify the possibility of the Weyl metal recently proposed for Mn₃Sn (ref. 11).

Mn₃Sn has a hexagonal crystal structure with a space group of $P6_3/mmc$ (ref. 23). Mn atoms form a breathing type of kagome lattice in the ab -plane (Fig. 1b), and the Mn triangles constituting

the kagome lattice are stacked on top along the c axis forming a tube of face-sharing octahedra. On cooling below the Néel temperature of 430 K, Mn magnetic moments of $\sim 3\mu_B$ lying in the ab -plane form a coplanar, chiral magnetic structure characterized by $Q=0$ wavevector, as clarified by the previous neutron diffraction studies^{24,25}. The combination of geometrical frustration and Dzyaloshinskii–Moriya interaction leads to the inverse triangular spin structure with uniform vector chirality (Fig. 1b)^{24–26}. The chiral antiferromagnetic order has orthorhombic symmetry and thus induces a very tiny magnetization $\sim 2 \text{ m}\mu_B$ per Mn, which is essential to switch the non-collinear antiferromagnetic structure by using magnetic field. On further cooling below ~ 50 K, a cluster-glass phase appears as spins cant toward [0001] (c axis)^{25,27,28}. In this study, we used two as-grown single crystals that have a single phase of hexagonal Mn₃Sn (ref. 29) (Methods and Supplementary Information), with slightly different compositions, that is, Mn_{3.06}Sn_{0.94} for Sample 1, and Mn_{3.09}Sn_{0.91} for Sample 2 (Methods). Hereafter, we focus on the coplanar magnetic phase at $T > 60$ K.

We first provide clear evidence of the large anomalous Hall and Nernst effects observed in Samples 1 and 2. Figure 2a,b shows the field dependence of the Hall resistivity $\rho_H(B)$ in $B \parallel [01\bar{1}0]$ for Samples 1 and 2, respectively. Clearly, there is a sharp jump in $\rho_H(B)$ with a small coercivity of < 200 G. In particular for Sample 2, the size of the jump $\Delta\rho_H$ reaches $\sim 9 \mu\Omega \text{ cm}$ at 100 K, which would be equivalent to the Hall resistivity due to an ordinary Hall effect under about a few hundred Tesla for free conduction electrons with density of order one electron per Mn atom. To make comparison with theory later, here we take the x , y and z coordinates along $[2\bar{1}\bar{1}0]$, $[01\bar{1}0]$ and $[0001]$, and estimate the Hall conductivity employing the expression that takes care of the anisotropy of longitudinal resistivity (Supplementary Fig. 1), namely, $\sigma_{ji} \approx -\rho_{ji}/(\rho_{ij}\rho_{ii})$, where $(i, j) = (x, y)$, (y, z) , (z, x) (ref. 21) (Supplementary Information). Figure 2c,d shows $-\sigma_{zx}$ versus B for Samples 1 and 2, respectively. The zero-field value is $\sim 50 \Omega^{-1} \text{ cm}^{-1}$ at 300 K for both samples and it becomes particularly enhanced for Sample 2 at low temperatures and reaches $120 \Omega^{-1} \text{ cm}^{-1}$ at 100 K. The sign change in the Hall effect as a function of field should come from the flipping of the tiny uncompensated moment that follows the rotation of the sublattice moments^{10,24,26}.

Our main experimental observation of a large ANE at room temperature is provided in Fig. 3a. The Nernst signal (transverse thermopower) $-S_{zx}$ of Sample 1 shows a clear rectangular hysteresis with an overall change of $\Delta S_{zx} \sim 0.7 \mu\text{VK}^{-1}$ as a function of the in-plane field. This is significantly large for an antiferromagnet and comparable to the values reported for ferromagnets, as we will

¹Institute for Solid State Physics, University of Tokyo, Kashiwa 277-8581, Japan. ²RIKEN-CEMS, 2-1 Hirosawa, Wako 351-0198, Japan. ³PRESTO, Japan Science and Technology Agency (JST), 4-1-8 Honcho Kawaguchi, Saitama 332-0012, Japan. ⁴CREST, Japan Science and Technology Agency (JST), 4-1-8 Honcho Kawaguchi, Saitama 332-0012, Japan. [†]These authors contributed equally to this work. [★]e-mail: satoru@issp.u-tokyo.ac.jp

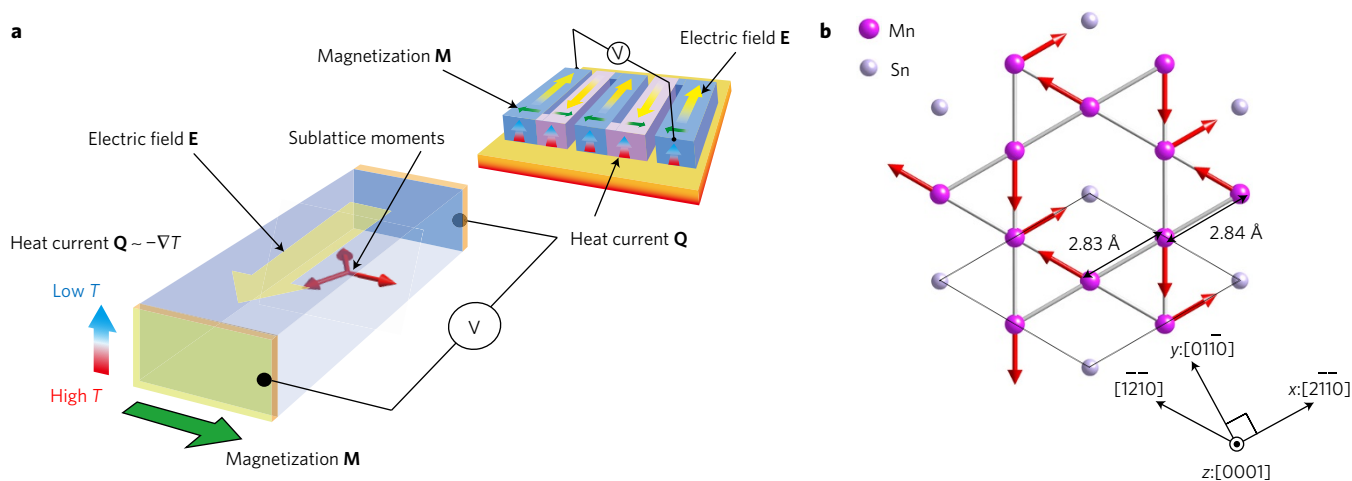


Figure 1 | Thermoelectric module using the anomalous Nernst effect, and crystal and magnetic structures of Mn_3Sn . **a**, Schematic illustration of a thermoelectric module based on the anomalous Nernst effect. The anomalous Nernst electric field \mathbf{E} appears in the direction of the outer product of the magnetization \mathbf{M} and heat current $\mathbf{Q} \sim -\nabla T$, and thus can be described as $\mathbf{E} = Q_s \mu_0 \mathbf{M} \times -\nabla T$, where Q_s is the anomalous Nernst coefficient and μ_0 is vacuum permeability. For the case of Mn_3Sn , the configuration of the sublattice moments is schematically presented. Inset: schematic illustration of a thermopile made of an array of magnetic modules. The in-plane magnetization directions of neighbouring thermoelectric modules are alternated so that the Nernst signal with the same sign can be added up in series. The heat flows along the direction perpendicular to the basal plane of the heat source. **b**, An individual ab -plane of Mn_3Sn . Spheres represent Mn (purple) and Sn (grey) atoms. In addition to the unit cell frame, Mn atoms are connected by lines to illustrate that they form a breathing type of kagome lattice (alternating array of small and large triangles). Mn moments (arrow) form an inverse triangular spin structure with uniform vector chirality on each Mn triangle.

discuss. While the in-plane Nernst signal exhibits hysteresis with almost no anisotropy, the out-of-plane c -axis component is zero within experimental accuracy, indicating no spontaneous effect in this direction. To further characterize the ANE, we compare it with the magnetization M by plotting in Fig. 3a both $-\alpha_{xx}$ and M sharing an x axis for the in-plane field. In low fields, the hystereses in both data almost overlap on top of each other. On the other hand, in the higher field region than the coercivity of ~ 100 G, the Nernst effect remains nearly constant, while M increases linearly with field as the sublattice moments cant toward the external field direction. These indicate negligible contributions from both the normal Nernst effect and the conventional ANE. Furthermore, the remnant Nernst signal at zero field is nearly the same as the saturated value in high field, demonstrating that the single-domain crystal has a large spontaneous Nernst signal as the first case for an antiferromagnet. Similar behaviour was found in the field cycles made for Sample 2 (Fig. 3b). A systematic change of the Nernst signal was observed with varying T for both Samples 1 and 2, (Fig. 3c,d). For Sample 1, the Nernst signal peaks at ~ 200 K, reaching a value of $0.6 \mu\text{V K}^{-1}$, comparable to the maximum value known for a ferromagnetic metal at room temperature⁷, while Sample 2 shows a smaller value, peaking at 250 K with $0.3 \mu\text{V K}^{-1}$. A distinct mechanism from the ferromagnetic case should be at work here as the spontaneous M in Mn_3Sn is nearly 1,000 times smaller than ordinary ferromagnets.

To further characterize thermoelectric properties, we measured the longitudinal Seebeck coefficient S_{ii} as a function of T and B . No field dependence was seen in S_{ii} for both samples in the T and B range of the measurements (Supplementary Information and Supplementary Fig. 2a,b). The Seebeck coefficient for Sample 1 positively peaks at ~ 300 K (Fig. 3c, inset), and takes a minimum value with a negative sign around 50 K. This minimum coincides with the steep rise in the specific heat, and thus, this sign change in $S(T)$ may be related to the effect of phonon drag that typically occurs at $\sim \Theta_D/5$, where Θ_D is the Debye T (Supplementary Information and Supplementary Fig. 3). Much reduced or no low T sign change was seen for Sample 2 (Fig. 3d, inset).

Generally, temperature gradient ∇T in an open-circuit condition is known to produce longitudinal and transverse electric field \mathbf{E} ,

which can be expressed as $\mathbf{J} = \boldsymbol{\sigma} \cdot \mathbf{E} + \boldsymbol{\alpha} \cdot (-\nabla T) = 0$. Here \mathbf{J} , $\boldsymbol{\sigma}$ and $\boldsymbol{\alpha}$ are the current density, electrical conductivity tensor, and thermoelectric conductivity tensor, respectively. This contains the transverse electric field coming from the thermal Hall effect, which should be negligible as it is usually one order of magnitude smaller than other contributions^{3,4,30}. Assuming this, the Nernst signal can be expressed as $S_{ij} = \rho_{ij}(\alpha_{ji} - S_{ii}\sigma_{ji})$, using the Seebeck coefficient $S_{ii}(=S)$ and the Hall conductivity $\sigma_{ji}(=\sigma_H)$. For this analysis, we used the T dependence of the Hall conductivity shown in Fig. 3e. As shown in Fig. 3c,d, $-\rho\alpha_{ji}$ estimated using this relation is found to be larger than $-S_{ii}$. We further estimated the transverse thermoelectric conductivity $-\alpha_{zx}$ versus T (Fig. 3f), which shows a systematic increase on cooling and has the maximum at $T \sim 150(100)$ K for Sample 1(2). At low temperatures, Sample 2 has twice smaller values than Sample 1. In ferromagnets, α_{ji} normally shows an increase on cooling, scaling linearly with M , and decreases linearly with T after M saturates^{3,4}. In Mn_3Sn , however, no correlation with M was seen in $-\alpha_{zx}(T)$ (Fig. 3f).

To further demonstrate the qualitative difference between the ANE observed in Mn_3Sn and in ferromagnets, we made a full logarithmic plot of the anomalous Nernst signal versus the magnetization for various ferromagnetic metals and Mn_3Sn (Fig. 4 and Methods). Here, the absolute values of the Nernst signal were taken in the magnetically ordered states of each material, and were plotted using B and T as implicit parameters. Similarly to AHE¹⁶, the ANE for ferromagnets is known to be proportional to magnetization. Figure 4 confirms that the overall trend for a broad range of ferromagnetic metals is for the anomalous Nernst signal to become larger with increasing magnetization (Methods). The shaded region that covers all of the data points indicates that the anomalous Nernst signal is indeed roughly proportional to the magnetization M , that is, $|S_{ij}| = |Q_s| \mu_0 M$ with the anomalous Nernst coefficient $|Q_s|$ ranging between 0.05 and $1 \mu\text{V K}^{-1} \text{T}^{-1}$. Following this relation, Mn_3Sn would have produced the Nernst signal of the order of $0.01 \sim 2 \text{ nV K}^{-1}$ with the observed magnetization. Strikingly, however, $S_{ij} \sim 0.3 \mu\text{V K}^{-1}$ found at room T is more than 100 times larger than what would be expected based on the above scaling relation for ferromagnets.

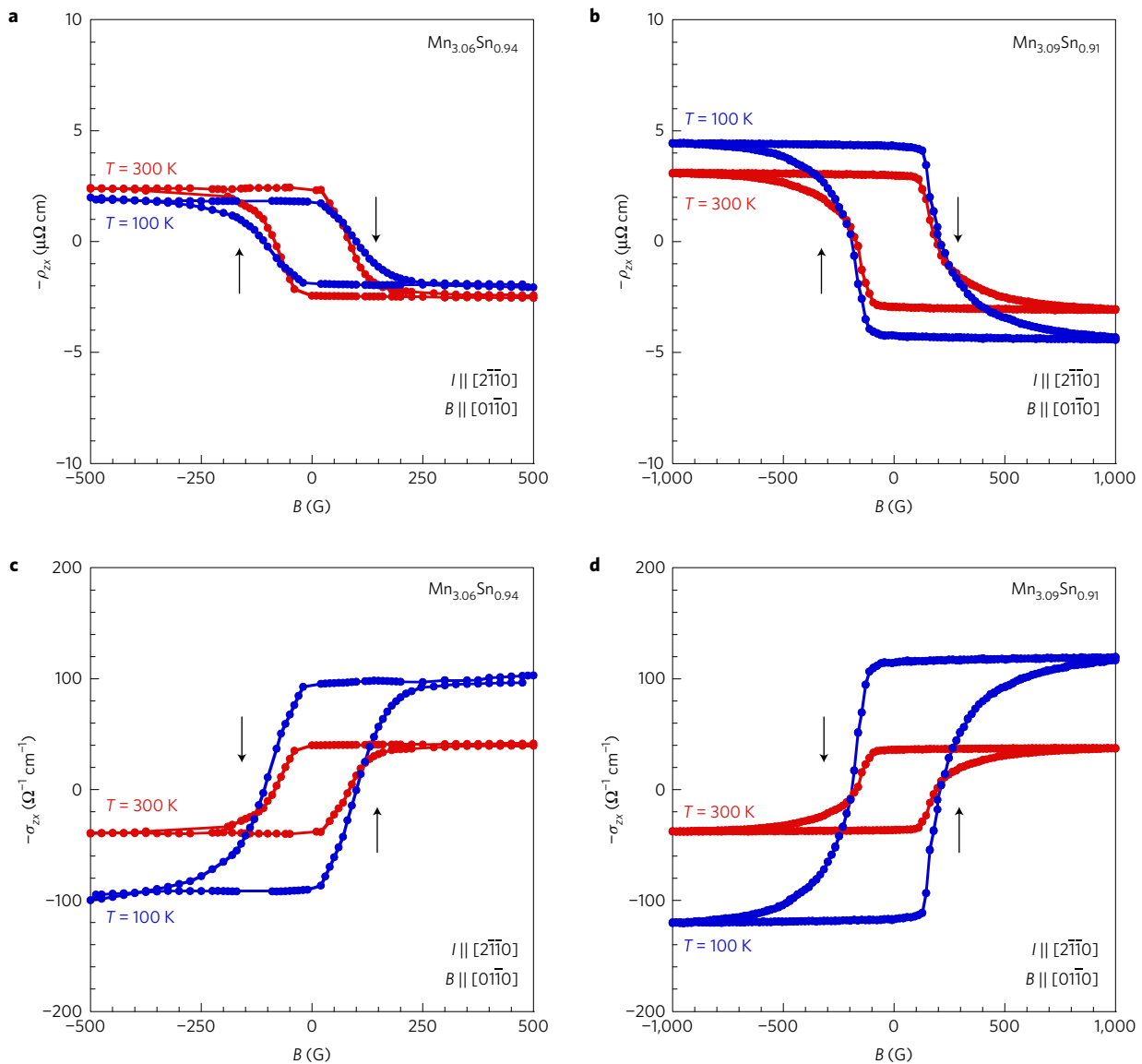


Figure 2 | Magnetic field dependence of the anomalous Hall effect in Mn_3Sn . **a,b**, Field dependence of the Hall resistivity $\rho_H = -\rho_{zx}$ of Sample 1 ($\text{Mn}_{3.06}\text{Sn}_{0.94}$) (**a**) and Sample 2 ($\text{Mn}_{3.09}\text{Sn}_{0.91}$) (**b**), obtained at 100 K, and 300 K. **c,d**, Field dependence of the Hall conductivity $\sigma_H = -\sigma_{zx}$ of Sample 1 (**c**) and Sample 2 (**d**) obtained at 100 K, and 300 K.

The significantly large anomalous Nernst and Hall effects in Mn_3Sn do not follow their conventional scaling relation with M , and thus it is natural to assume that both effects arise through the same mechanism distinct from the conventional one for ferromagnets. The inverse triangular spin structure for Mn_3Sn reduces the lattice symmetry from six-fold to two-fold in the plane and thus based on the symmetry argument, the Hall effect may appear in the ab -plane^{10,31}. Indeed, a recent calculation found that Mn_3Sn may have a large anomalous Hall conductivity²⁰, which can be estimated by integrating the Berry curvature of the occupied bands over the entire Brillouin zone⁹. More recently, the possibility of a Weyl metal has been proposed, where the bands crossing E_F have several Weyl points, around which the Berry curvature diverges¹¹.

Another intriguing quantity governed by the Berry curvature is the anomalous Nernst effect. While all of the occupied bands are relevant for the anomalous Hall conductivity, only the Berry curvature around the Fermi level determines the ANE or, more precisely, the transverse thermoelectric conductivity α_{ji} (refs 8,9). Therefore, α_{ji} is significantly enhanced when the Berry curvature takes a large value at E_F . To see this in the case of Mn_3Sn , we performed

a first-principles calculation, confirming the Weyl points nearby E_F (ref. 11). The calculated anomalous Hall conductivity $-\sigma_{zx}$ is found as large as seen in experiment. Theoretically, the extra Mn in Sample 1(2) should dope the conduction electron (Supplementary Information) and thus increase E_F by 0.04 (0.05) eV. Since $-\sigma_{zx}$ forms a peak at $E - E_F \sim 0.065$ eV (Supplementary Fig. 4), a shift in E_F from +0.04 to +0.05 eV leads to a slight increase in $-\sigma_{zx}$, but a substantial decrease in $-\alpha_{zx}$ (Fig. 3e,f inset). This behaviour is consistent with the experimental observation, that is, Mn doping suppresses $-\alpha_{zx}$ by 50% at low temperatures, while it enhances $-\sigma_{zx}$ only by $\sim 10\%$ (Fig. 3e,f). For a simple Weyl Hamiltonian, σ_{ji} takes its maximum and α_{ji} becomes zero when E_F is located exactly at the Weyl node and on the other hand, α_{ji} becomes strongly enhanced when E_F moves slightly away³². Clearly, the real band structure of Mn_3Sn should be more complicated. Interestingly, however, our theory also finds that $-\sigma_{zx}$ forms a peak at $E - E_F \sim 0.065$ eV, around which Weyl nodes exist¹¹, and $-\alpha_{zx}$ becomes large when E_F is slightly away from the nodes (Supplementary Fig. 4). Our results thus indicate that the ANE in Mn_3Sn is particularly enhanced because of the characteristic structure of the Berry curvature with

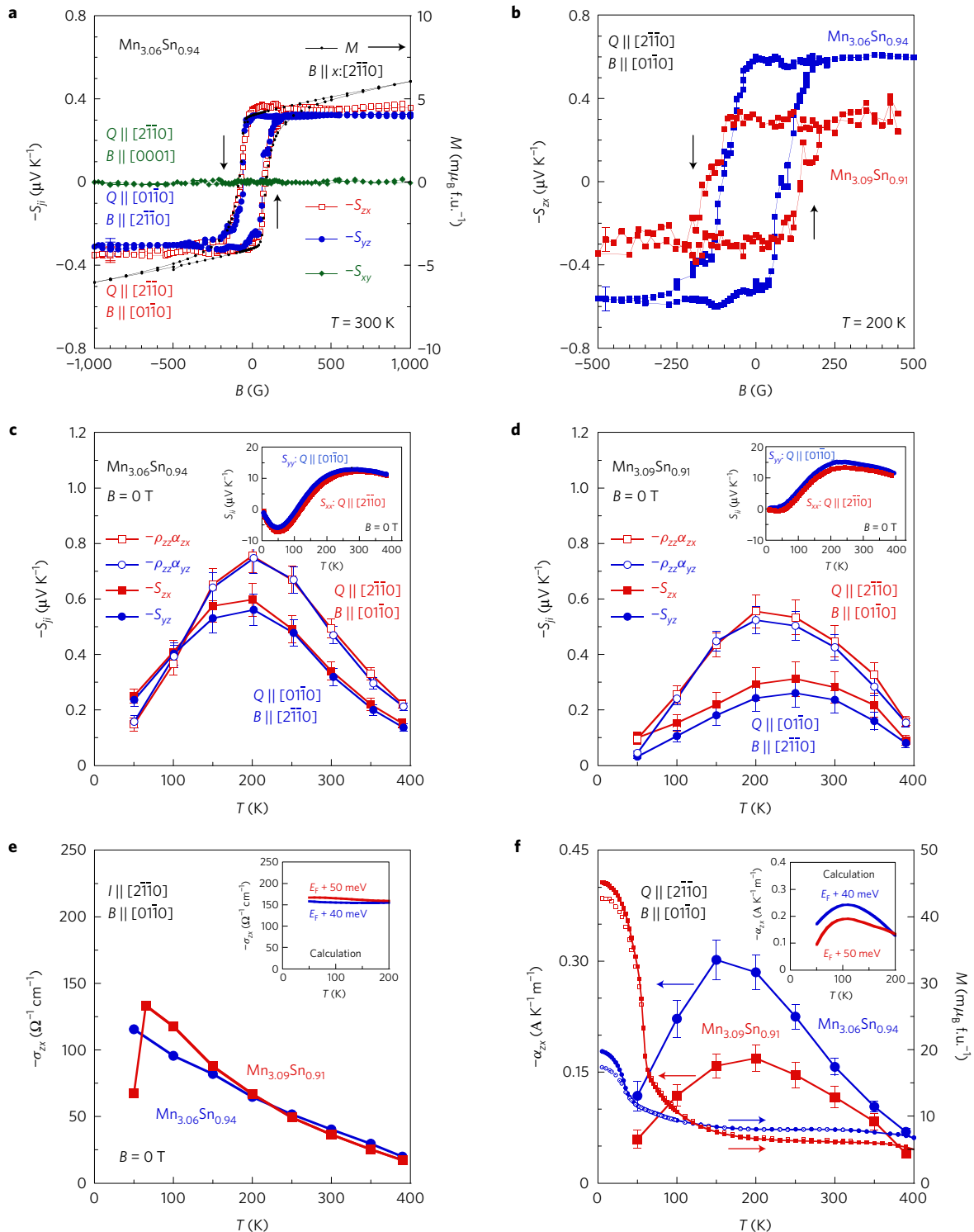


Figure 3 | Anomalous Nernst effect in Mn_3Sn . **a**, Anisotropic field dependence of the Nernst signal $-S_{ji}$ of Sample 1. For comparison, the field dependence of the magnetization M (right axis) for $B \parallel x$ is shown. **b**, $-S_{zx}$ versus B of Samples 1 and 2 measured at 200 K. Here, Samples 1 and 2 refer to crystals with $\text{Mn}_{3.06}\text{Sn}_{0.94}$ and $\text{Mn}_{3.09}\text{Sn}_{0.91}$, respectively. **c, d**, T dependence of the zero-field remnant Nernst signal S_{ji} (filled symbols) obtained by the field sweep measurements of Sample 1 (**c**) and Sample 2 (**d**). The thermoelectric contribution estimated using the relation $\rho_{jj}\alpha_{jj} = S_{ji} - S_{ii}(\rho_{ji}/\rho_{ii})$ is also shown (open symbols). Insets: Seebeck coefficients S_{xx} , S_{yy} versus T measured under zero field for Sample 1 (**c**) and Sample 2 (**d**). **e**, Hall conductivity $-\sigma_{zx}$ versus T estimated using the relation $\sigma_{zx} = -\rho_{zx}/(\rho_{xx}\rho_{zz})$. The sudden drop in $-\sigma_{zx}$ for Sample 2 is due to the magnetic transition at ~ 60 K (see **f**). Inset: $-\sigma_{zx}$ versus T for $E - E_F = +40$ (blue) and $+50$ (red) meV obtained by the first-principles calculation. **f**, Transverse thermoelectric conductivity $-\alpha_{zx}$ versus T (left axis), estimated using the relation, $\alpha_{zx} = (S_{zx}/\rho_{zz}) + \sigma_{zx}S_{xx}$ for the field sweep results (filled circles ($\text{Mn}_{3.06}\text{Sn}_{0.94}$) and filled squares ($\text{Mn}_{3.09}\text{Sn}_{0.91}$)). For comparison, the T dependences of M (right axis) obtained in $B = 1,000$ G $\parallel y$ using field-cooling (FC, filled symbols) and zero-field-cooling (ZFC, open symbols) sequences are shown. The FC and ZFC results bifurcate at ~ 50 (60) K for Sample 1 (2) due to the magnetic transition. Inset: $-\alpha_{zx}$ versus T for $E - E_F = +40$ (blue) and $+50$ (red) meV obtained by the first-principles calculation. The error bars are shown if they are larger than the symbol sizes and indicate the measurement errors that come from the uncertainties of their geometrical factors (Methods).

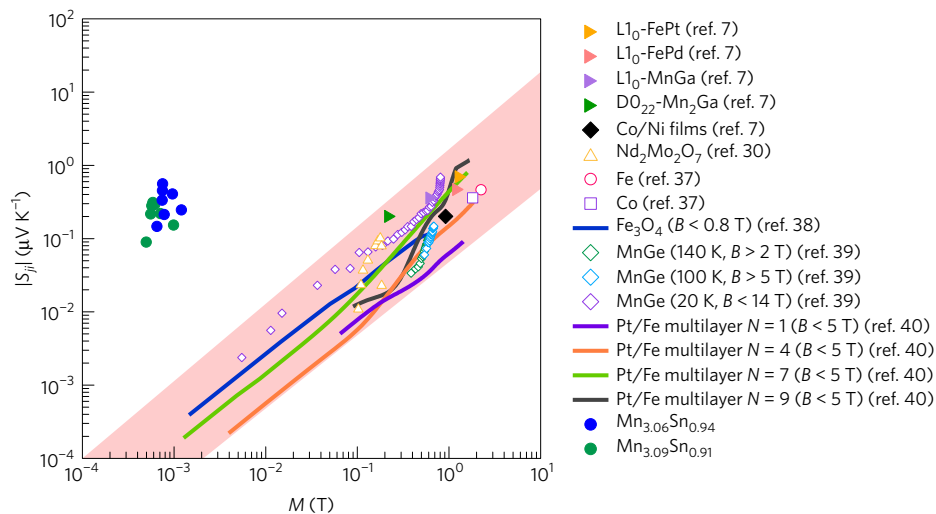


Figure 4 | Magnetization dependence of the spontaneous Nernst effect for ferromagnetic metals and Mn_3Sn . Full logarithmic plot of the anomalous Nernst signal $|S_{ji}|$ versus the magnetization M for a variety of ferromagnetic metals and Mn_3Sn measured at various temperatures and fields (Methods). It shows the general trend for ferromagnets that $|S_{ji}|$ increases with M . The shaded region indicates the linear relation $|S_{ji}| = |Q_s| \mu_0 M$, with $|Q_s|$ ranging from $\sim 0.05 \mu V K^{-1} T^{-1}$ to $\sim 1 \mu V K^{-1} T^{-1}$. The Nernst signal data points obtained at various temperatures for Sample 1 ($Mn_{3.06}Sn_{0.94}$) for $B \parallel [01\bar{1}0]$ and for Sample 2 ($Mn_{3.09}Sn_{0.91}$) (blue filled circles) for $B \parallel [01\bar{1}0]$ (green filled circle) do not follow the relation, and reach almost the same value as the largest among ferromagnetic metals with three orders of magnitude smaller M .

several Weyl points nearby the Fermi level^{11,32}. Our study further highlights the complementary roles of anomalous Hall conductivity σ_{ji} and transverse thermoelectric conductivity α_{ji} in revealing the topological character of band structure.

Finally, from the viewpoint of application for thermoelectric power generation, ANE could be useful as it facilitates the fabrication of a module structurally much simpler than the conventional one using the Seebeck effect⁶. The orthogonal orientation of the voltage output to the thermal heat flow (Fig. 1a) enables a lateral series connection of a single kind of ferromagnet with alternating magnetization direction (Fig. 1a inset). This simplifies a thermopile structure to efficiently cover the surface of a heat source (Fig. 1a inset), in comparison with the conventional thermoelectric module using the Seebeck effect, which consists of a pillar structure of alternating p- and n-type semiconductors. To increase power density, a thermopile should ideally cover the entire surface of a heat source, and therefore, a micro-fabricated thermopile array has to be arranged as densely as possible. However, as long as a ferromagnet is used, their inherent stray fields may perturb magnetization direction of neighbouring modules, and limit the integration density.

Our discovery of a new class of material that produces almost no stray fields but exhibits a large ANE is highly important for the application toward thermoelectric power generation, and it should allow us to design a thermopile with a much denser integration of thermoelectric modules to efficiently cover a heat source than the ferromagnetic counterparts. While the observed values in this work would be still far from the size necessary for application, our study indicates that the magnetic Weyl metals such as Mn_3Sn should be particularly useful to obtain a larger ANE by enhancing the Berry curvature at E_F . Further studies to develop the technology for application such as thin-film growth and coercivity control of such magnets will be important to build a thermoelectric power generator.

Methods

Methods, including statements of data availability and any associated accession codes and references, are available in the [online version of this paper](#).

Received 6 June 2016; accepted 23 May 2017;
published online 24 July 2017

References

- Smith, A. W. The transverse thermomagnetic effect in nickel and cobalt. *Phys. Rev.* **33**, 295–306 (1911).
- Kondorskii, E. I. & Vasileva, R. Degree of localization of magnetic electron and the Nernst–Etingshausen effect in ferromagnetic metals. *Sov. Phys. JEPT* **18**, 277–278 (1964).
- Lee, W.-L., Watauchi, S., Miller, V. L., Cava, R. J. & Ong, N. P. Anomalous Hall heat current and Nernst effect in the $CuCr_2Se_{4-x}Br_x$ ferromagnet. *Phys. Rev. Lett.* **93**, 226601 (2004).
- Miyasato, T. *et al.* Crossover behavior of the anomalous Hall effect and anomalous Nernst effect in itinerant ferromagnets. *Phys. Rev. Lett.* **99**, 086602 (2007).
- Pu, Y., Chiba, D., Matsukura, F., Ohno, H. & Shi, J. Mott relation for anomalous Hall and Nernst effects in $Ga_{1-x}Mn_x$ As ferromagnetic semiconductors. *Phys. Rev. Lett.* **101**, 117208 (2008).
- Sakuraba, Y. *et al.* Anomalous Nernst effect in $L1_0$ -FePt/MnGa thermopiles for new thermoelectric applications. *Appl. Phys. Express* **6**, 033003 (2013).
- Hasegawa, K. *et al.* Material dependence of anomalous Nernst effect in perpendicularly magnetized ordered-alloy thin films. *Appl. Phys. Lett.* **106**, 252405 (2015).
- Xiao, D., Yao, Y., Fang, Z. & Niu, Q. Berry-phase effect in anomalous thermoelectric transport. *Phys. Rev. Lett.* **97**, 026603 (2006).
- Xiao, D., Chang, M.-C. & Niu, Q. Berry phase effects on electronic properties. *Rev. Mod. Phys.* **82**, 1959–2007 (2010).
- Nakatsuji, S., Kiyohara, N. & Higo, T. Large anomalous Hall effect in a non-collinear antiferromagnet at room temperature. *Nature* **527**, 212–215 (2015).
- Yang, H. *et al.* Topological Weyl semimetals in the chiral antiferromagnetic materials Mn_3Ge and Mn_3Sn . *New J. Phys.* **19**, 015008 (2017).
- Bauer, G. E. W., Saitoh, E. & van Wees, B. J. Spin caloritronics. *Nat. Mater.* **11**, 391–399 (2012).
- Uchida, K. *et al.* Observation of the spin Seebeck effect. *Nature* **455**, 778–781 (2008).
- Slachter, A., Bakker, F. L., Adam, J.-P. & van Wees, B. J. Thermally driven spin injection from a ferromagnet into a non-magnetic metal. *Nat. Phys.* **6**, 879–882 (2010).
- Huang, S. Y., Wang, W. G., Lee, S. F., Kwo, J. & Chien, C. L. Intrinsic spin-dependent thermal transport. *Phys. Rev. Lett.* **107**, 216604 (2011).
- Nagaosa, N., Sinova, J., Onoda, S., MacDonald, A. H. & Ong, N. P. Anomalous Hall effect. *Rev. Mod. Phys.* **82**, 1539–1592 (2010).
- Bruno, P. in *Handbook of Magnetism and Advanced Magnetic Materials* Vol. 1 (eds Kronmuller, H. & Parkins, S.) Ch. 22, 540–558 (John Wiley, 2007).

18. Machida, Y., Nakatsuji, S., Onoda, S., Tayama, T. & Sakakibara, T. Time-reversal symmetry breaking and spontaneous Hall effect without magnetic dipole order. *Nature* **463**, 210–213 (2010).
19. Chen, H., Niu, Q. & MacDonald, A. H. Anomalous Hall effect arising from noncollinear antiferromagnetism. *Phys. Rev. Lett.* **112**, 017205 (2014).
20. Kübler, J. & Felser, C. Non-collinear antiferromagnets and the anomalous Hall effect. *Europhys. Lett.* **108**, 67001 (2014).
21. Kiyohara, N., Tomita, T. & Nakatsuji, S. Giant anomalous Hall effect in the chiral antiferromagnet Mn_3Ge . *Phys. Rev. Appl.* **5**, 064009 (2016).
22. Nayak, A. K. *et al.* Large anomalous Hall effect driven by a nonvanishing Berry curvature in the noncollinear antiferromagnet Mn_3Ge . *Sci. Adv.* **2**, e1501870 (2016).
23. Krén, E., Paitz, J., Zimmer, G. & Zsoldos, É. Study of the magnetic phase transformation in the Mn_3Sn phase. *Physica B* **80**, 226–230 (1975).
24. Tomiyoshi, S. & Yamaguchi, Y. Magnetic structure and weak ferromagnetism of Mn_3Sn studied by polarized neutron diffraction. *J. Phys. Soc. Jpn* **51**, 2478–2486 (1982).
25. Brown, P. J., Nunez, V., Tasset, F., Forsyth, J. B. & Radhakrishna, P. Determination of the magnetic structure of Mn_3Sn using generalized neutron polarization analysis. *J. Phys. Condens. Matter.* **2**, 9409–9422 (1990).
26. Nagamiya, T., Tomiyoshi, S. & Yamaguchi, Y. Triangular spin configuration and weak ferromagnetism of Mn_3Sn and Mn_3Ge . *Solid State Commun.* **42**, 385–388 (1982).
27. Tomiyoshi, S., Abe, S., Yamaguchi, Y., Yamauchi, H. & Yamamoto, H. Triangular spin structure and weak ferromagnetism of Mn_3Sn at low temperature. *J. Magn. Mater.* **54–57**, 1001–1002 (1986).
28. Feng, W. J. *et al.* Glassy ferromagnetism in Ni_3Sn -type $\text{Mn}_{3.1}\text{Sn}_{0.9}$. *Phys. Rev. B* **73**, 205105 (2006).
29. Ohmori, H., Tomiyoshi, S., Yamauchi, H. & Yamamoto, H. Spin structure and weak ferromagnetism of Mn_3Sn . *J. Magn. Mater.* **70**, 249–251 (1987).
30. Hanasaki, N. *et al.* Anomalous Nernst effects in pyrochlore molybdates with spin chirality. *Phys. Rev. Lett.* **100**, 106601 (2008).
31. Suzuki, M.-T., Koretsune, T., Ochi, M. & Arita, R. Cluster multipole theory for anomalous Hall effect in antiferromagnets. *Phys. Rev. B* **95**, 094406 (2017).
32. Sharma, G., Goswami, P. & Tewari, S. Nernst and magnetothermal conductivity in a lattice model of Weyl fermions. *Phys. Rev. B* **93**, 035116 (2016).
33. Weischenberg, J., Freimuth, F., Blügel, S. & Mokrousov, Y. Scattering-independent anomalous Nernst effect in ferromagnets. *Phys. Rev. B* **87**, 060406 (2013).
34. Ramos, R. *et al.* Anomalous Nernst effect of Fe_3O_4 single crystal. *Phys. Rev. B* **90**, 054422 (2014).
35. Shiomi, Y., Kanazawa, N., Shibata, K., Onose, Y. & Tokura, Y. Topological Nernst effect in a three-dimensional skyrmion-lattice phase. *Phys. Rev. B* **88**, 064409 (2013).
36. Uchida, K. *et al.* Enhancement of anomalous Nernst effects in metallic multilayers free from proximity-induced magnetism. *Phys. Rev. B* **92**, 094414 (2015).

Acknowledgements

We thank A. Nugroho, A. Sakai, T. Higo and N. Kiyohara for useful discussions. This work is partially supported by CREST (Grant Number JPMJCR15Q5) and PRESTO, Japan Science and Technology Agency, and Grants-in-Aid for Scientific Research (16H02209), and Program for Advancing Strategic International Networks to Accelerate the Circulation of Talented Researchers (No. R2604) from the Japanese Society for the Promotion of Science, and by Grants-in-Aids for Scientific Research on Innovative Areas (15H05882, 15H05883, 26103002) of the Ministry of Education, Culture, Sports, Science, and Technology of Japan. The use of the facilities of the Materials Design and Characterization Laboratory at the Institute for Solid State Physics, The University of Tokyo, is gratefully acknowledged.

Author contributions

S.N. and Y.O. conceived the project. S.N. planned the experiments, and T.T., M.I. and S.N. performed experiments and analysed data. T.K., M.-T.S. and R.A. performed the first-principles calculations. D.N.-H. performed the TEM measurements and analyses. S.N. and R.A. wrote the main text. M.I., S.N., T.T., D.N.-H., T.K., M.-T.S. and R.A. prepared the Supplementary Information and figures; all authors discussed the results and commented on the manuscript.

Additional information

Supplementary information is available in the online version of the paper. Reprints and permissions information is available online at www.nature.com/reprints. Publisher's note: Springer Nature remains neutral with regard to jurisdictional claims in published maps and institutional affiliations. Correspondence and requests for materials should be addressed to S.N.

Competing financial interests

The authors declare no competing financial interests.

Methods

Polycrystalline samples were made by melting the mixtures of manganese and tin in an alumina crucible sealed in an evacuated quartz ampoule in a box furnace at 1,050 °C for 6 h. In preparation for single-crystal growth, the obtained polycrystalline materials were crushed into powders, compacted into pellets, and inserted into an alumina crucible that was subsequently sealed in an evacuated silica ampoule. Single-crystal growth was performed using a single-zone Bridgman furnace with a maximum temperature of 1,080 °C and growth speed of 1.5 mm h⁻¹. Analysis using inductively coupled plasma spectroscopy showed that the composition of the single crystal is Mn_{3.06}Sn_{0.94} for Sample 1 and Mn_{3.09}Sn_{0.91} for Sample 2. Powder X-ray diffraction measurement was performed using a diffractometer (RAPID, Rigaku) with a rotating stage to remove preferred orientation in the data. The one-dimensional intensity pattern was extracted from two-dimensional Debye–Scherrer rings that were obtained using transmission mode. Rietveld analysis was performed using RIETAN-FP. All of the samples were shown to be single phase, with lattice parameters consistent with previous work (see Supplementary Information and Supplementary Tables 1 and 2). After the alignment made using Laue diffractometer, the as-grown single crystals were cut into bar-shaped samples by spark machining for transport and magnetization measurements.

The magnetization measurements were done using a commercial SQUID magnetometer (MPMS, Quantum Design). The associated measurement error is less than a few per cent. The specific heat measurement was performed using a commercial system (PPMS, Quantum Design) under zero magnetic field (Supplementary Information). Both longitudinal and Hall resistivities were measured by a standard four-probe method using a commercial system (PPMS, Quantum Design). Electrical contacts were made by spot-welding gold wires for the longitudinal and transverse voltage probes, both of which were placed ~1.5 mm apart on the sample with a typical current cross-section area of ~0.20 mm². In addition, thermoelectric properties were jointly measured by the one-heater and two-thermometer configuration using a commercial system (PPMS, Quantum Design). For thermoelectric measurements, the samples have the typical dimension of ~10 × 2 × 2 mm³ for Sample 1 (Mn_{3.06}Sn_{0.94}) and ~5 × 1.5 × 1.5 mm³ for Sample 2 (Mn_{3.09}Sn_{0.91}). The thermal gradient $-\nabla T$ was applied by a heater at one end of the bar-shaped sample toward a thermal bath at the other end, and was measured by monitoring two thermometers linked to the sample by strips of ~0.5-mm-wide copper–gold plates along the longest direction of the sample. The distance between the two thermometers is approximately ~5 mm for Sample 1 and ~2.5 mm for Sample 2. The magnitude of the transverse voltage ΔV was found to be linearly increasing with the increase of applied temperature difference ΔT . Here, ΔT was typically set to be 1.5% ~ 2.0% of the sample temperature for both Seebeck and Nernst measurements. By setting the temperature gradient $-\nabla T$ along a bar-shaped single crystal (i axis), the thermoelectric longitudinal and transverse emf voltages V_i and V_j were measured in an open-circuit condition. The Seebeck coefficient S_{ii} and Nernst signal S_{ji} were then estimated as $S_{ii} = E_i/\nabla T$ and $S_{ji} = E_j/\nabla T$, where E_i and E_j are the longitudinal and transverse electric field. The magnetic field dependence of the Hall resistivity and the Nernst signal was

obtained after removing the longitudinal component of the respective transport properties, which is found to be approximately constant as a function of the magnetic field (Supplementary Information).

The measurement errors for the longitudinal resistivity ρ_{ii} , Hall resistivity ρ_{ji} , and Nernst signal S_{ji} , are dominated by the uncertainties of their respective geometrical factors. The uncertainty of the longitudinal resistivity and Hall resistivity is 1–2% and smaller than the symbol sizes used in the figures in the main text and Supplementary Information. The uncertainty in the Nernst signal S_{ji} is ~10% for Sample 1 and ~20% for Sample 2. The corresponding error bars for the Nernst signal and the transverse thermoelectric conductivity are given in Fig. 3 and Supplementary Fig. 2.

The transverse thermoelectric conductivity α_{xx} was calculated using the Berry curvature formula⁸ with the first-principles electronic structure. The density functional theory calculation was performed within the generalized-gradient approximation³⁷ as implemented in the quantum-ESPRESSO package³⁸. A $7 \times 7 \times 7$ k -point grid, ultrasoft pseudopotentials³⁹ and plane wave basis sets with cutoff energies of 80 Ry for wavefunctions and 320 Ry for charge densities were used. For the Berry curvature calculation, a Wannier-interpolated band structure⁴⁰ with a $40 \times 40 \times 40$ k -point grid was employed.

The specimens for transmission electron microscopy were prepared by Ar ion milling using a JEOL Ion-Slicer operated at 5.5 kV and 150 μ A under a low beam angle of 2.5°. Selected-area electron diffraction and high-resolution lattice images were obtained using a transmission electron microscope (JEOL JEM-2010F) operated at 200 kV. High-resolution lattice images were simulated by MacTempas software.

Figure 4 was made using the ANE results obtained for various ferromagnets well below their Curie temperatures, as reported in the literature including Li₁₀-FePt (300 K; ref. 7), Li₁₀-FePd (300 K; ref. 7), Li₁₀-MnGa (300 K; ref. 7), D0₂₂-Mn₂Ga (300 K; ref. 7), Co/Ni films (300 K; ref. 7), Nd₂Mo₂O₇ ($T < T_c = 73$ K, $B = 1$ T || [111]; ref. 30), Fe (300 K; ref. 33), Co (300 K; ref. 33), Fe₃O₄ (300 K, $B < 0.8$ T; ref. 34), MnGe (140 K, $B > 2$ T; ref. 35), MnGe (100 K, $B > 5$ T; ref. 35), MnGe (20 K, $B < 14$ T; ref. 35), and Pt/Fe multilayer $N = 1 \sim 9$ (300 K, $B < 5$ T; ref. 36).

Data availability. The data that support the plots within this paper and other findings of this study are available from the corresponding author on reasonable request.

References

- Perdew, J., Burke, K. & Ernzerhof, M. Generalized gradient approximation made simple. *Phys. Rev. Lett.* **77**, 3865 (1996).
- Giannozzi, P. *et al.* Quantum espresso: a modular and open-source software project for quantum simulations of materials. *J. Phys. Condens. Matter* **21**, 395502 (2009).
- Vanderbilt, D. Soft self-consistent pseudopotentials in a generalized eigenvalue formalism. *Phys. Rev. B* **41**, 7892 (1990).
- Mostofi, A. A. *et al.* wannier90: a tool for obtaining maximally-localised Wannier functions. *Comput. Phys. Commun.* **178**, 685–699 (2008).